Materials Science & Engineering A 754 (2019) 719–727

Contents lists available at ScienceDirect

Materials Science & Engineering A

journal homepage: www.elsevier.com/locate/msea

Characterising the fatigue performance of additive materials using the small punch test

D.T.S. Lewis[a], R.J. Lancaster[a,*], S.P. Jeffs[a], H.W. Illsley[a], S.J. Davies[a], G.J. Baxter[b]

[a] Institute of Structural Materials, College of Engineering, Swansea University Bay Campus, Swansea, SA1 8EN, United Kingdom
[b] Rolls-Royce Plc., P.O. Box 31, Derby, DE24 8BJ, United Kingdom

ARTICLE INFO

Keywords:
Additive manufacturing
Small punch
Fatigue
Titanium alloys
Nickel based superalloys

ABSTRACT

In recent years the use of Additive Manufacturing (AM) has become increasingly widespread with numerous industries now moving towards large scale manufacture of structurally integral components. The nature of AM offers the ability to manufacture more complex and optimised geometries, such as cooling channels and honeycomb structures, which would not be possible or economically viable to manufacture using more traditional fabrication processes. However, the layer by layer build structure of AM components also introduces a complex and component specific microstructure arising from the rapid cooling rates resulting from the build parameters and geometries, which hence influence the mechanical properties. Therefore, the use of conventional mechanical test approaches to assess the performance of these materials can be limited. This paper will extend upon some of the recent research at Swansea University in applying the innovative small punch fatigue (SPF) experiment to characterise the mechanical performance of AM materials and how they compare to traditionally manufactured variants of the same alloys. Results show excellent agreement with the microstructural morphologies of the different materials, with supporting fractography evidencing the contrasting failure modes.

1. Introduction

Much research is now available that details the complexities of AM structures [1], and the difficulties in establishing appropriate methods for mechanical property assessment [2]. However, there remains a significant demand from industry to understand and characterise the performance limitations of these often intricately built structures. Some of the most recent mechanical test approaches have typically required either building a separate test specimen within the build volume or extracting one from within a fully built component. These methods, however, are inherently inadequate for characterising the local microstructure of small complex features due to the dependency of the properties on the geometry and volume constraints of the features which are of most interest. As such, miniaturised test techniques, such as the small punch (SP) test, have the unique potential to be utilised for this application where the ability to gather useful mechanical property data from small volumes of material is necessary. There is an extensive history of the use of SP test techniques dating back to the 1980s, including a plethora of applications in a range of industrial sectors [3–5]. In recent years, research has been targeted towards exploiting the potential of SP testing within the aerospace industry for characterising novel materials and processes where material quantities are limited [6]. Furthermore, the potential of the technique to evaluate the properties of AM materials has also been explored [7]. However, despite the progress and evolution of the test approach, SP testing has primarily been limited to characterising the tensile and creep properties of materials, with very little literature documenting the use of small scale testing to characterise fatigue properties [8,9]. Whilst acknowledging that fatigue is the predominant damage mechanism in metallic materials and is thought to account for 80–90% of in-service engine failures, an understanding of the fatigue properties of such components is necessary. Given the low material volume requirement and the ability to extract specimens from complex and component representative geometries, SP fatigue testing would be of tremendous benefit to the mechanical characterisation community. This paper will present a series of results across two alternative aerospace alloy systems to demonstrate the capability of this new mechanical test approach. Experimental data will be provided for Laser Powder Bed Fused (LPBF) nickel based superalloy C263 and Electron Beam Melted (EBM) titanium alloy Ti-6Al-4V, and how these materials compare to their traditionally manufactured counterparts to further validate the sensitivity of the SPF experiment in characterising dissimilar microstructures of the same

* Corresponding author.
E-mail addresses: d.t.s.lewis@swansea.ac.uk (D.T.S. Lewis), r.j.lancaster@swansea.ac.uk (R.J. Lancaster), s.p.jeffs@swansea.ac.uk (S.P. Jeffs), 634576@swansea.ac.uk (H.W. Illsley), 656258@swansea.ac.uk (S.J. Davies), gavin.baxter@rolls-royce.com (G.J. Baxter).

https://doi.org/10.1016/j.msea.2019.03.115
Received 25 January 2019; Received in revised form 26 March 2019; Accepted 27 March 2019
Available online 30 March 2019

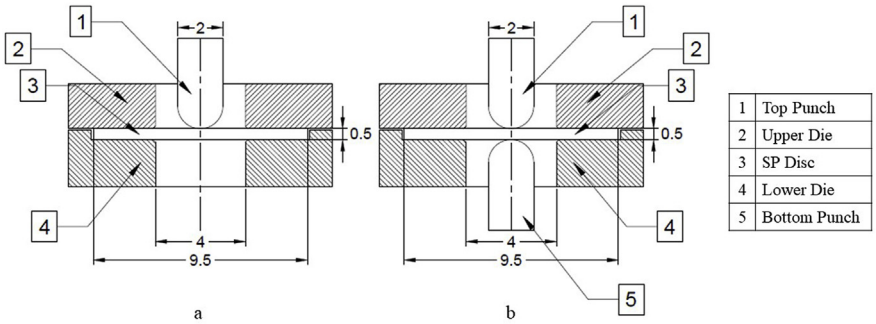

Fig. 1. Small punch fatigue test geometry for a) a single indenter arrangement for R = < 0 and b) a dual indenter system for R = < 0.

material. Supporting microstructural studies and fractography will provide evidence of the evolving fatigue damage in the miniature disc specimens, how failure contrasts between the different material types and how SP fatigue testing offers the capability of detecting such microstructural intricacies to rank the cyclic behaviour of these alloys.

2. Experimental procedures

2.1. Experimental set-up

A bespoke SP fatigue mechanical testing capability has been developed at Swansea University to test SP disc specimens at both ambient and elevated temperatures under sensitive loading conditions. The apparatus is designed to be inserted into the axial load train of a servo-hydraulic test frame, with a dedicated ± 5 kN load cell employed to ensure that load is controlled to high precision. The test configuration, as depicted in Fig. 1, either employs a single or dual indenter system, depending on the desired loading ratio (or R ratio). A single punch is used to apply a positive R ratio and a dual indenter system used to replicate fully reversed loading. In either set up, the punch indenter and enclosing die sets are made from Nimonic-90, with a LVDT employed to monitor disc displacement through the duration of the test. All dimensions conform to the European Code of Practise for SP Testing (EUCoP) [10] and the soon to published EN Standard for SP testing. Further details regarding the test set up can be found in Ref. [11].

2.2. Materials

In this research, two alternative material systems used for aerospace applications were assessed; titanium alloy Ti-6Al-4V and nickel based superalloy C263. These two materials were chosen for this research as several studies have already been performed on AM versions of the two alloys by the same authors [11–14]. Compositions for each are given in Tables 1 and 2.

2.2.1. Ti-6Al-4V variants

For Ti-6Al-4V, three different microstructural variants of the alloy were investigated; namely forged, cast & Hot-Isostatic-pressed (HIP) and Electron Beam Melted (EBM). The EBM material was built in a vertical orientation on an Arcam system configured with EBM Control 3.2 Service Pack software. The pre-alloyed plasma atomised Ti-6Al-4V powder feedstock contained spherical particles ranging from 45 to 105 μm in diameter. The first layer of powder was deposited onto a 220 × 300 × 10 mm^3 thick stainless steel base plate that was pre-heated with the electron beam to approximately 730 °C. Prior to melting each layer, the new layer of powder was preheated and sintered by scanning the beam over the cross-sectional geometry in an attempt to maintain a consistent build temperature of 730 °C throughout and reduce the effects of powder charging during melting. Further information regarding this process can be found in Ref. [15]. Inverse Pole Figure (IPF) maps of the Z-plane for all three variants are presented in Fig. 2, which shows the transverse (X-Y) plane in each instance. Here, the transverse plane represents the microstructure which is subjected to SP loading.

Table 1
Composition of Ti-6Al-4V (wt%).

Ti	Al	V	C	O	N	H	Fe
Bal	6	4	0.1	0.2	0.05	0.012	0.25

Table 2
Composition of C263 (wt%).

Ni	Co	Cr	Mo	Al	Ti	C	B	Zr
Bal	20	20	5.9	0.5	2.1	0.06	0.001	0.02

2.2.2. C263 variants

A total of five C263 variants were assessed in this research. This included the cast equivalent of the alloy and four Laser Powder Bed Fused (LPBF) materials, built in two perpendicular build orientations and exposed to either one of two heat treatment regimes. The LPBF variants were built using an EOS M270 machine from gas atomised powder, with a powder size distribution of 40–100 μm. Parameters that are broadly in line with industry standards although considered proprietary. Two of the materials were built in a horizontal (or 0°) orientation and two in a vertical (or 90°) direction. Two specimens from each orientation were then exposed to two alternative heat treatment programmes. The first heat treatment, otherwise termed HT1, consisted of the standard heat treatment schedule for C263, of 2 h solution heat treatment at 1150 °C, followed by 8 h ageing treatment at 800 °C [16]. The second heat treatment regime, or HT2, was an experimental heat treatment schedule including a higher temperature solution heat treatment of 1275 °C [12]. This higher temperature was implemented to recrystallise the microstructure and alleviate the as built texture. Deposition parameters were identical across all four of the LPBF builds. The cast material in this study was also subjected to HT1 for comparative purposes. Fig. 3 and 4 display the IPF-Z plane maps of the five materials investigated, as previously seen in Ref. [13], and reproduced here for ease of comparison. Grain size data measurements for each of the Ti-6Al-4V and C263 materials are listed in Tables 3 and 4. Given the biaxial nature of the test along with the anisotropy typically seen in AM materials, aspect ratios of the grain morphologies were determined from a minimum of 250 grains. Aspect ratio provides the ellipsoidal form of the grains as defined by the mean linear intercept method, to calculate the ratio of the width to the height. Due to the strong bimodal nature of the microstructure observed in the C263 cast material, two average grain size values are provided to reflect the newly recrystallised grains and the predominantly larger grains. To ensure statistically reliable measurements, a series of optical micrographs were captured for

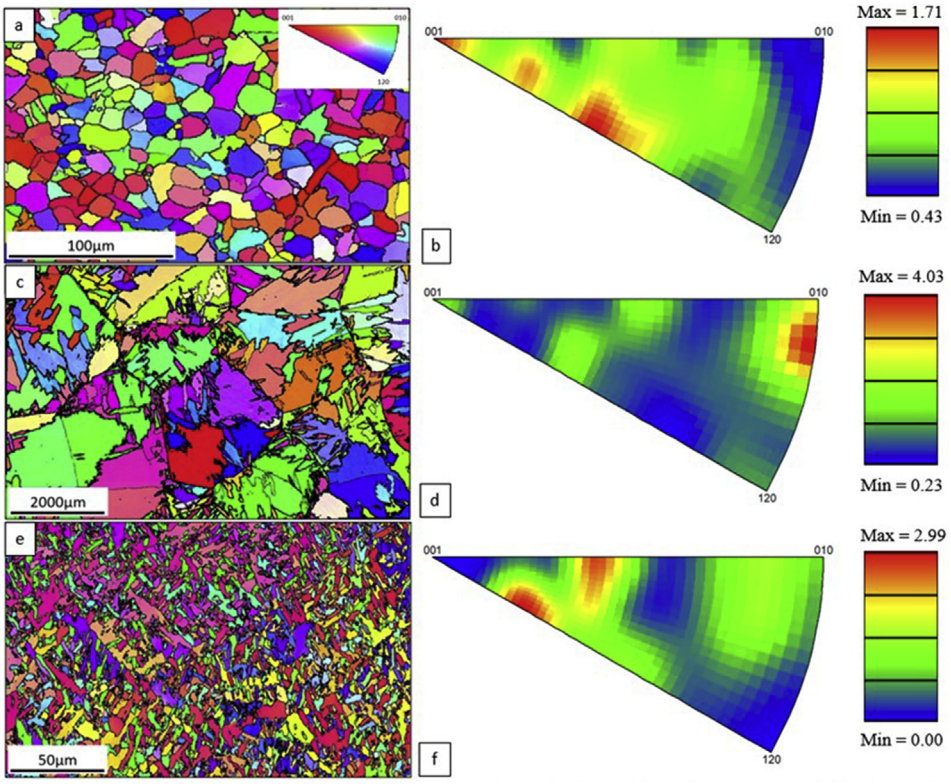

Fig. 2. Inverse pole figure maps and Z-IPFs of the transverse (X–Y) plane for Ti-6Al-4V a) b) forged, c) d) cast & HIP and e) f) EBM.

each variant and selected areas were scanned using Electron Backscatter Diffraction (EBSD), conducted on a Hitachi SU3500 Scanning Electron Microscope (SEM) operated at 20 kV and 100 μA. The mean linear intercept method was used in all cases with the exception of the cast variants, due to the bimodal size distribution, and the HT1 0° C263 material due to its anisotropic columnar grain structure. In these cases, the elliptical fit method was utilised.

2.3. Specimens

SP specimens were extracted from the threaded ends of conventional tensile specimens for forged and EBM Ti-6Al-4V and the four C263 LPBF variants. Each of the threads were reduced to 9.5 mm diameter rods. The material for cast & HIP Ti-6Al-4V and cast C263 was extracted from larger pieces into 9.5 mm diameter rods by wire electrical discharge machining (EDM). All of the rods were then sectioned into 0.8 mm thick slices. The slices all sections were ground and polished down to the required thickness of 500 μm ± 5 μm using progressively finer grades of silicon carbide abrasive paper, the final grade being 1200 grit in accordance with the EUCoP recommendations [10]. The final disc thickness was checked for uniformity by measuring five locations around the periphery and the centre of the specimen. Any samples that lied outside this tolerance were rejected.

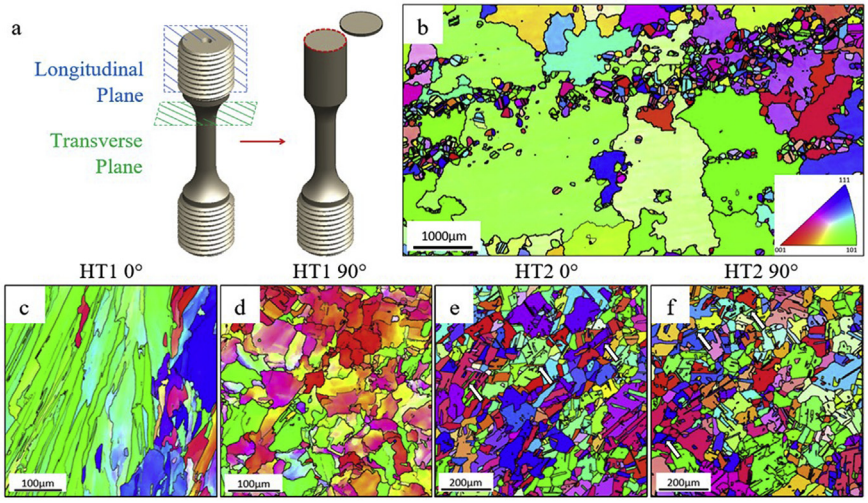

Fig. 3. Reproduced inverse pole figure maps of the transverse (X–Y) plane for C263 a) uniaxial specimen planes and SP disc extraction b) cast, c) HT1 0°, d) HT1 90°, e) HT2 0°, f) HT2 90° [15].

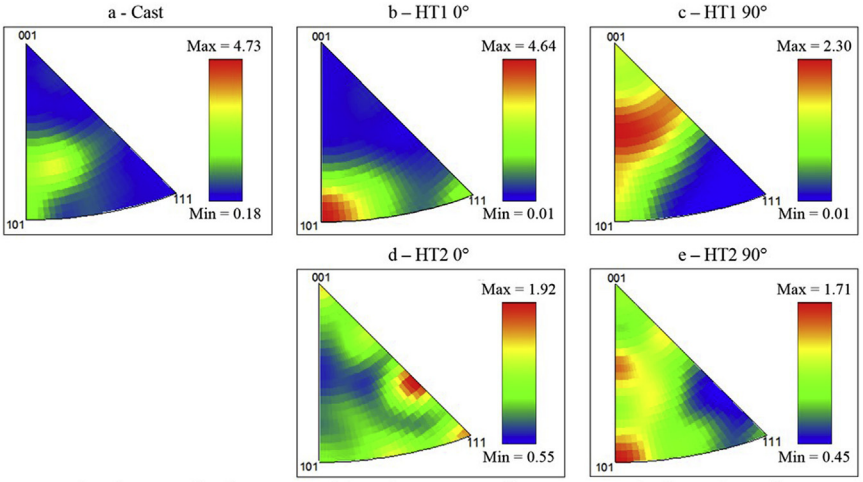

Fig. 4. Reproduced Z-IPFs of each C263 materials variant, corresponding to IPF maps in Fig. 3; a) cast, b) HT1 0°, c) HT1 90°, d) HT2 0°, e) HT2 90° [15].

Table 3
Grain size measurements for Ti-6Al-4V variants.

Ti-6Al-4V Variant	Average Grain Size [μm]	Aspect Ratio
Cast	57.23	0.33
Forged	3.41	0.52
EBM	1.29	0.51

Table 4
Grain size measurements for C263 variants.

C263 Variant	Average Grain Size [μm]	Aspect Ratio	Σ3 [%]
Cast	101.74/921.83	0.55/0.52	29.0
HT1 0°	29.58	0.23	0.158
HT1 90°	22.79	0.99	0.005
HT2 0°	52.02	0.94	67.6
HT2 90°	57.79	0.94	67.7

3. Results & discussion

3.1. F_{MAX} v N_f behaviour

A series of SP fatigue tests were performed on each of the Ti-6Al-4V and C263 variants to generate a relationship between maximum force (F_{MAX}) versus number of fatigue cycles to failure (N_f). The experiments on Ti-6Al-4V were performed under force control with a loading ratio of $R = -1$ to simulate a fully reversed loading cycle with a compressive portion, whereas all tests on C263 employed an R ratio of 0.1 to give a near zero to maximum response to eliminate any cycling effects through zero force. All tests across the two materials were performed at 20 °C using a 1 Hz sinusoidal waveform. The tests were stopped after a total displacement of 250 μm was achieved on either side of the SP disc. This criterion was established from a series of preliminary trials, where it was found beyond 250 μm, a clearly defined crack could be identified.

Fig. 5 presents the SPF test results in the form of F_{MAX} against N_f for all tests on Ti-6Al-4V. It should be noted that all of the curves have high R^2 values, highlighting the consistency of the test method. The trendlines for the conventionally manufactured material variants have R^2 values > 0.95, whereas the R^2 value for the EBM material is 0.90. The lower R^2 value for the EBM data suggests more variability in the fatigue behaviour of this material than for the conventionally manufactured variants, as would be expected when considering the anisotropic and transient nature of the EBM microstructure (Fig. 2e). Despite the small scatter in the EBM results, the material appears to offer a marginally stronger fatigue performance, thought to be predominantly linked to the finer grain size compared to the other materials. In contrast, the coarser grained cast material is revealed to be the least resistant of the three variants to SP fatigue (Fig. 2c). When considering the grain morphologies for the three materials, as given in Table 3, the EBM variant would be expected to have a far superior fatigue performance given the vastly refined microstructure in accordance with Hall-Petch theory. Therefore, additional factors controlling the fatigue behaviour must be considered. Previous literature has highlighted that the fatigue properties of EBM parts without post-manufacture HIP are influenced by the presence of porosity [17,18]. Published research by the authors [14] found that the EBM material used in this study is 99.97% fully dense as established through X-ray computed tomography (XCT). As such, the cross-sectional thickness of the load bearing material is slightly reduced in the EBM variant in comparison to forged and cast materials, which were 100% dense, leading to an expected marginal debit in the fatigue capabilities of the EBM material despite exhibiting a finer grain size. Furthermore, the EBM material can be argued to have a marginally greater volume of texture in the microstructure compared to the forged equivalent, as shown by the Z-IPFs in Fig. 2. However, given the vastly different size of the grains across the three materials, texture is not believed to have a major impact on the resulting fatigue performance.

Fig. 6 displays the results from the SPF tests on the C263 variants, all of which were performed under an R ratio of 0.1. The results show that the SPF test has a clear sensitivity to the various grain structures produced via the different manufacturing procedures. An improvement in yield strength through the Hall-Petch relationship [19] has resulted in improvements in the F_{MAX} values for similar SPF lives achieved in the variants with smaller grain sizes, which in this case is seen in the LPBF C263 materials.

Whereas for Ti-6Al-4V, the EBM material was found to have the most scatter, here, the cast C263 clearly has the least established trend. This relates to the bimodal microstructure (Fig. 3b) of the cast material and can explain the vast differences seen in the F_{MAX} v N_f curve. Yet, even though the HT1 builds exhibit the smallest grain sizes, the greater fatigue lives for a given load were seen in the HT2 variants. Previous studies by the authors [14] found a similar trend when evaluating the small punch tensile (SPT) performance of the same materials [12], where the HT1 materials achieved a higher degree of displacement compared to HT2, even though the F values were similar. This behaviour can likely be attributed to the abundance of annealing twins (otherwise known as Σ3s) present in the HT2 material (examples indicated by the arrows on Fig. 3) which can provide a strengthening effect on a given material by hindering slip. Furthermore, it has been reported in the literature that by raising the solution heat treatment

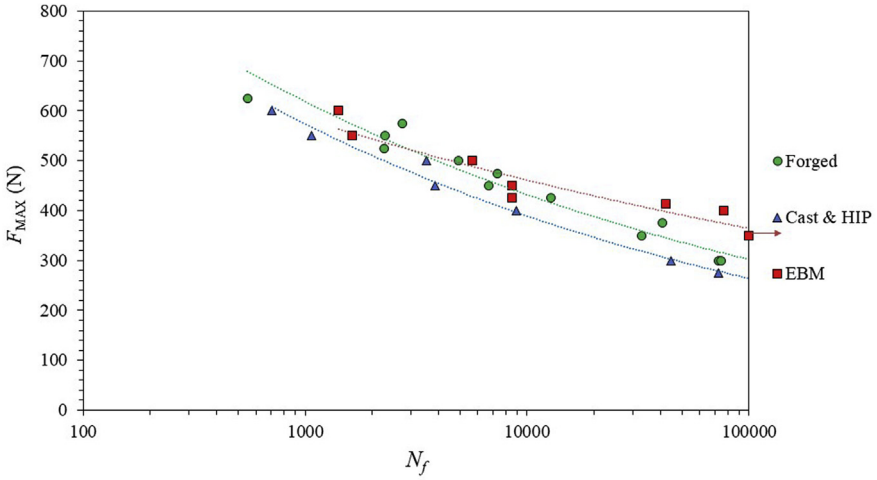

Fig. 5. F_{MAX} v N_f response for Ti-6Al-4V variants, R = −1, 20 °C.

temperature to temperatures in excess of the γ′ solvus temperature (925 °C), an increase in γ′ size and volume fraction is expected [20,21]. Though γ′ coarsening has not been observed at this level, a diminished presence of Ti and Al segregates between HT1 and HT2 conditions has been witnessed by the authors in previous research [13], with these elements likely contributing to γ′ precipitation [22], and thus acting to further strengthen the HT2 variants. Additionally, the eradicated texture seen in HT2 variants (Fig. 3) will act to inhibit any crack propagation during SPF testing, in comparison to HT1 variants where neighbouring grains have lower misorientation.

When analysing the LPBF SPF results, it appears that much of the anisotropy in the HT1 C263 materials has been supressed by the biaxial nature of the SP test. However, there is a noticeable difference in the behaviour of the HT2 builds where the 0° variant outperforms the 90° equivalent, even though they appear to hold comparable equiaxed microstructures as previously seen (Fig. 3). This potentially can be attributed to a number of factors. Firstly, a slightly finer grain size is seen in the 0° orientation (52.02 μm for 0° compared to 57.70 μm for 90°) [13]. Schmid factors were also obtained in directions predicted relating to membrane stretching in a typical SP test configuration [23] and the 90° variant was found to have marginally higher factors across both X (0.450–0.448) and Y planes (0.470–0.445). This suggests that slip is likely to be active at lower loads, as appears to be the case in the 90° material and corroborated by the SPT results, where the HT2 0° material shows a greater magnitude of ductility prior to failure compared to the 90° equivalent [12]. One final influence could be that finer γ′ sizes are typically found near the top surface of an AM build [24]. When considering the geometry of consolidated uniaxial test pieces, finer γ′ is then expected to be present in a larger proportion of the 90° variant compared to a specimen built in the 0° orientation.

3.2. Force-displacement behaviour

In addition to the F_{MAX} v N_f results, force-displacement loops were generated for each of the tests to replicate hysteresis strain-stress behaviour typically recorded in uniaxial fatigue test arrangements. Fig. 7 presents the monotonic and 1000th loops recorded from the R = −1 tests on the different Ti-6Al-4V materials under the same load, whilst the same loops for the R = 0.1 SPF results for C263 are given in Fig. 8.

The force-displacement loops depicted in Fig. 7 were generated under an applied F_{MAX} of 500 N. The figure highlights the high level of consistency achieved across the three tests from the regularity of the maximum and minimum loads reached in each. The asymmetry in loading and unloading during the tests show the accumulation of plastic deformation in the specimens over the duration of the experiments. A considerable amount of non-recoverable plastic deformation, represented here as displacement, occurs in the monotonic cycle as the load applied is sufficient to initiate the membrane stretching deformation mode in the SP specimen. This behaviour is akin to that observed in SPT tests [14,25]. After this initial cycle, the increase in

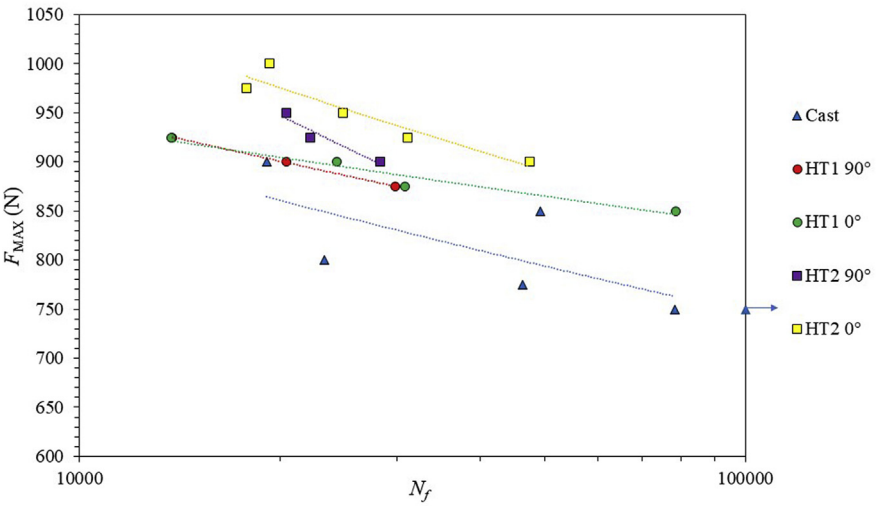

Fig. 6. F_{MAX} v N_f response for C263 variants, R = 0.1, 20 °C.

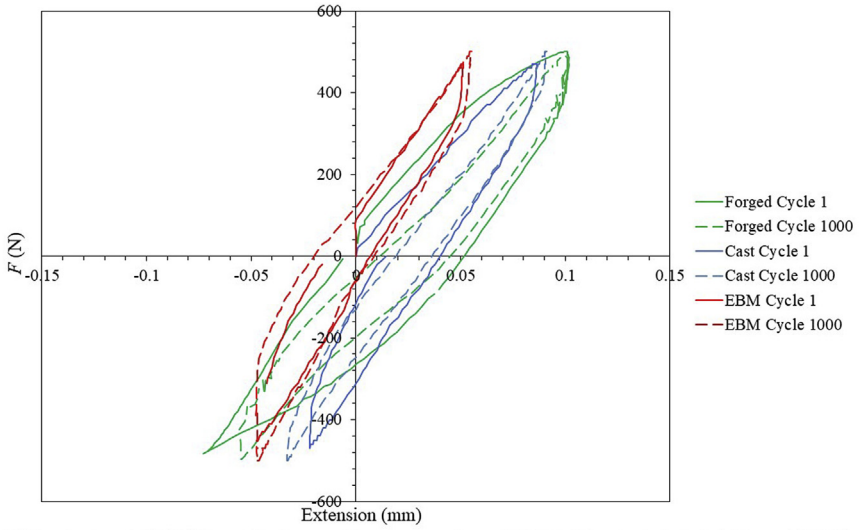

Fig. 7. Monotonic and 1000th Load-Displacement Loop comparison of Ti-6Al-4V variants tested at F_{MAX} = 500 N, R = −1, 20 °C.

maximum and minimum displacement begins to stabilise and then becomes more incremental, a phenomenon referred to in more traditional fatigue as ratcheting [26]. The hysteresis behaviour for the three materials compare favourably with the F_{MAX} v N_f performance, as the EBM material experiences the smallest degree of plastic deformation (~20 μm compared to ~50 μm in forged and ~40 μm in cast) on the first cycle, leading to the longest life of the three specimens given in this comparison (N_f = 5675, compared to N_f = 4900 for forged and N_f = 3525 for cast).

The force-displacement loops for the C263 variants were tested under R = 0.1, F_{MAX} = 900 N. Fig. 8 further highlights that the consistency achieved in this test arrangement for a fully reversed R ratio is excellent, with repeatable maximum and minimum loads. The width of the monotonic loop, or the level of initial plastic deformation, for the cast variant is the largest when comparing the five materials and the level of displacement by which the 1000th loop has drifted from the initial monotonic position further indicates the level of permanent damage accumulated by the cast material. This is favourable with the F_{MAX} v N_f curves seen in Fig. 6 where the cast material performed the worst. On the contrary, given the lack of deformation seen in the HT1 builds, these would be expected to have the best performance. However, as discussed previously, the superior lives of the HT2 materials is attributed to a number of influencing microstructural and crystallographic factors.

3.3. Small punch fatigue (SPF) fractography

Following testing, the fracture surfaces of each of the specimens were assessed. Fig. 9 presents the fracture morphology for the forged and EBM Ti-6Al-4V specimens, both of which were tested under R = −1 and F_{MAX} = 650 N. In both instances, the discs are dominated by a star-like cracking morphology with the cracks growing in a radial manner from the central region of the disc, akin to a brittle type of deformation typically seen in SPT tests [7]. This is similar to that seen in the F_{MAX} v N_f curves given in Fig. 5, with the two materials showing little contrast in behaviour. As the discs accumulate an increasing number of SPF cycles, crack growth becomes more extensive, stretching the membrane further until it is unable to withstand the applied force. Across both material types, there is limited evidence of characteristic fatigue markings on the fracture surfaces. The absence of such features is due to damage caused as the load transitions through zero from positive to negative, thus closing and re-opening the crack and abrading the fracture surface, as is the case for uniaxial fatigue tests under an R = −1 loading regime.

A further understanding of the crack behaviour can be gathered when analysing the crack morphologies of the different variants. Fig. 10

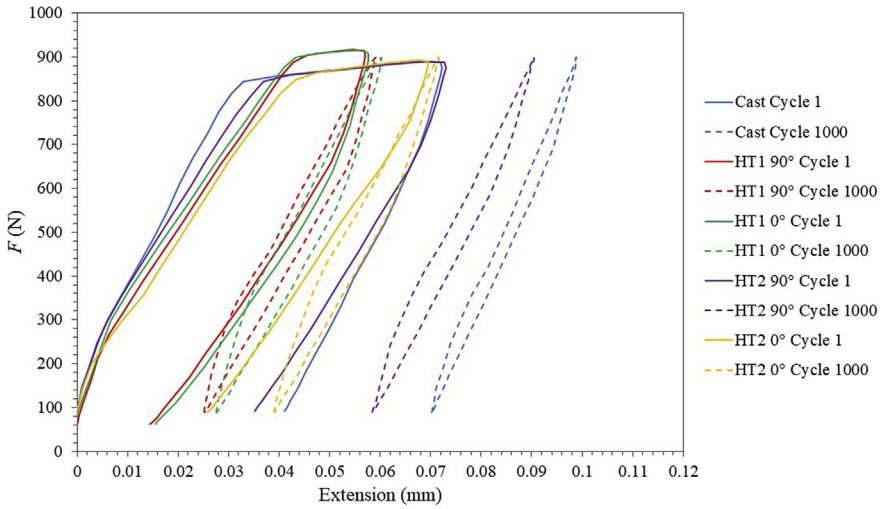

Fig. 8. Monotonic and 1000th Load-Displacement Loop Comparison of C263 variants tested at F_{MAX} = 900 N, R = 0.1, 20 °C.

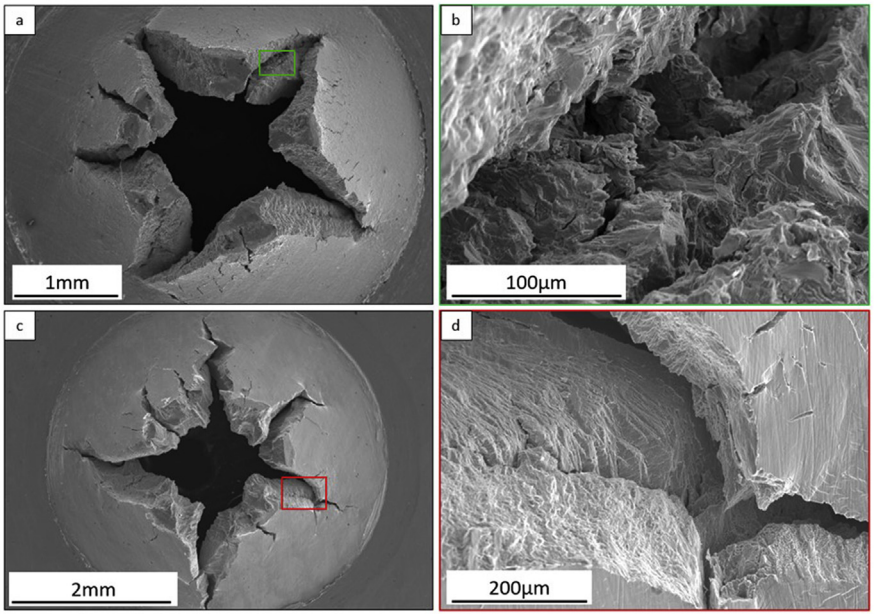

Fig. 9. SPF fractographic images of Ti-6Al-4V tested at F_{MAX} = 500 N, R = −1, 20 °C a), b) forged, c), d) EBM.

shows the contrasting nature of crack growth for the three Ti-6Al-4V materials. The crack path propagation mechanism observed in the forged material (Fig. 10a) is mixed mode, where the crack propagates predominantly in a transgranular manner while also interacting with neighbouring grain boundaries with the microstructure providing little impediment to crack growth. The nature of crack growth through the microstructure of the cast & HIP specimen, as shown in Fig. 10b, is seen to be mostly transgranular, with the grain boundaries of the large prior β grains having minimal effect on the direction of the crack path. The growing crack propagates in a manner irrespective of the presence of prior β grain boundaries and α laths in this variant. This was previously observed to be the case during crack path analysis of cast & HIP Ti-6Al-4V specimens following SP tensile testing [14].

The crack behaviour through the EBM microstructure, shown in Fig. 10c, is more complex than for the other two material variants. Here the crack can be seen be travelling in a transgranular manner through the columnar prior β grains but the effect of the α laths is less clear. The crack growth deviates around many of the acicular α laths and propagates in an inter-lath manner.

A contrasting mode of failure can be seen in Fig. 11, which shows the fracture surfaces for cast and HT2 0° C263 variants. The discs were subjected to an R = 0.1 waveform, eliminating any possible effects of cycling through zero, and F_{MAX} = 900 N. In these tests, additional features were present that can be directly attributed to fatigue damage. These markings are striations, which under more traditional uniaxial fatigue test arrangements represent the increment of crack growth that occurs in a single loading cycle through the plastic blunting process. These can be seen in both the cast alloy and the HT2 0° LPBF material, giving confidence of the experimental process under a positive loading cycle. Previous work by the authors studied the presence of striations that were observed on fracture surfaces under SPF loading and found a strong correlation between the number of striation features and the

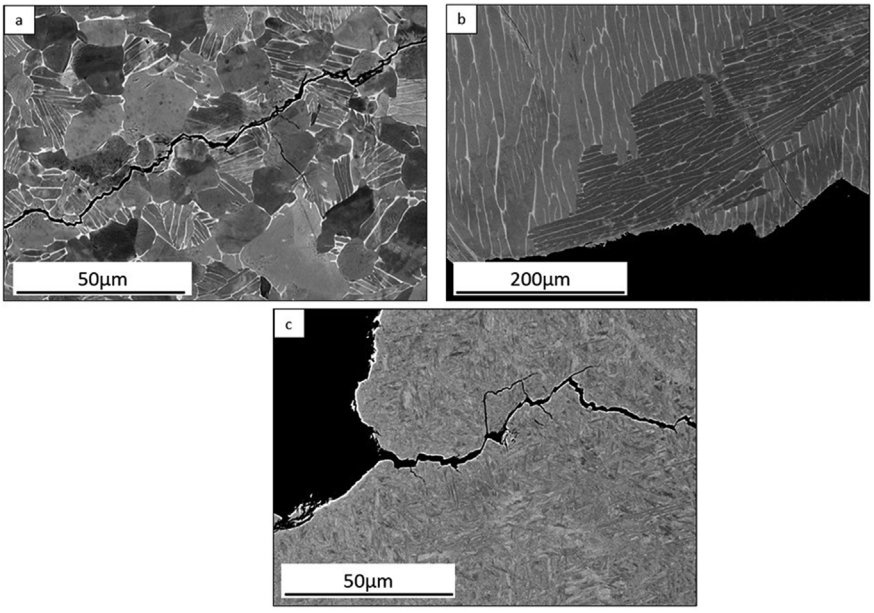

Fig. 10. Crack path morphologies for a) forged, b) cast & HIP and c) EBM Ti-6Al-4V variants tested at F_{MAX} = 500 N, R = −1, 20 °C.

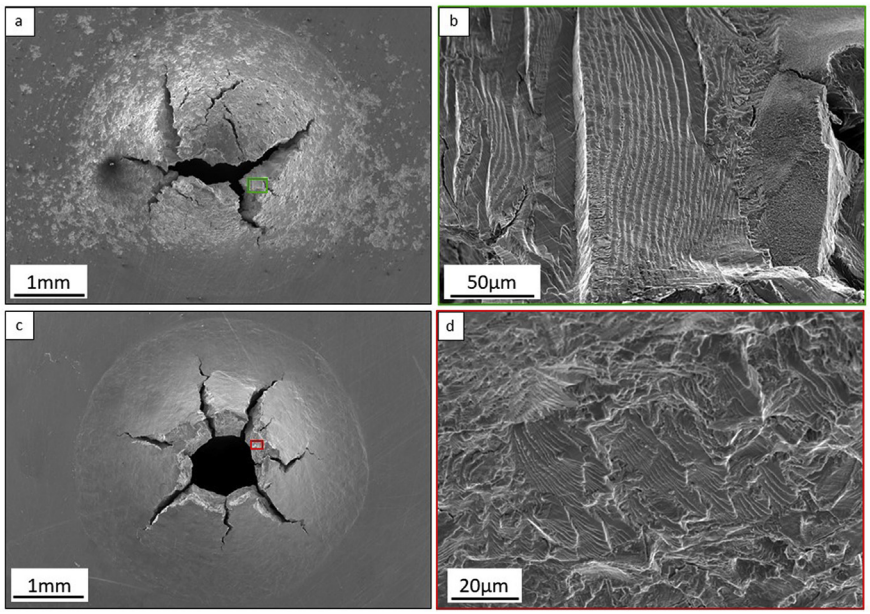

Fig. 11. SPF fractographic images of C263 tested at F_{MAX} = 900 N, R = 0.1, 20 °C a), b) cast, c), d) LPBF HT2 0°.

Table 5
Average striation spacing for C263 variants subjected to a load of 900 N.

C263 Variant	Average Striation Spacing (µm)
Cast	2.29
HT1 0°	1.11
HT1 90°	0.82
HT2 0°	0.76
HT2 90°	0.77

total number of cycles to failure [11]. Whereas striations usually develop from a surface or slightly sub-surface location under uniaxial testing, here, they develop from the central region (or the crack origin) and progress perpendicularly outwards from the advancing crack in a concentric manner. Striation spacing increases with increasing distance from the centre of the specimen, giving a clear indication of the direction of the propagating crack and the rate at which the crack is progressing. This behaviour is synonymous with fatigue damage under more recognised testing approaches. Average striation spacing values were calculated for the five C263 materials subjected to a load of 900 N. Using the same procedure detailed in Ref. [11], a series of images were taken of the fracture surfaces for each sample and five measurements were taken of the width of 10 striations using ImageJ image processing and analysis software. From these measurements, the mean striation width was calculated and are displayed in Table 5. The spacing of the striations follows the same pattern seen in the F_{MAX} v N_f plot in Fig. 6, where the strongest performing variant, HT2 0°, exhibited the most closely spaced striations, reflecting the slowest rate of crack growth. Whereas in contrast, the cast material had the most widely spaced striations, therefore the faster rate of crack propagation and worst fatigue response for an applied load of 900 N.

4. Conclusions

In this study, a novel small punch fatigue test capability has been employed to characterise the fatigue properties of additive manufactured aerospace materials and how they compare to their traditionally manufactured equivalents. From this work, the following conclusions have been drawn:

- The Small Punch Fatigue test has successfully ranked the fatigue performance of three Ti-6Al-4V variants that were manufactured through alternative processes including Electron Beam Melting and four Laser Powder Bed Fused C263 builds in comparison to the cast material.
- The fatigue behaviour of the eight materials has been attributed to the inherent microstructural morphologies of the different variants. The cast equivalents of both Ti-6Al-4V and C263 are composed of the largest grain size and hence an inferior fatigue performance, whereas the more refined grain structures, as seen in Electron Beam Melted and Laser Powder Bed Fused materials, exhibit a superior response.
- In the LPBF variants, several other microstructural and crystallographic factors must be considered as they are also thought to play an influencing role. The superior SPF performance seen in HT2 materials can be directly attributed to the alleviation of texture, an increased presence of annealing twins and a reduction in the Kernal Average Misorientation angles compared to the HT1 variants.
- The contrasting behaviours of the HT2 builds is believed to be related to a slight increase in grain size (10%) and γ′ content, with a reduction in the relevant Schmid factors for the 0° build compared to the 90° orientation.
- Fractographic investigations have revealed that typical fatigue striations are present on discs subjected to positive loading ratios, with their distance increasing with incremental crack growth. This information provides an effective insight into the rate of crack propagation, as the spacing of striations revealed that crack growth is three times faster in the cast variant compared to the HT2 0° equivalent under similar loading conditions. This behaviour is consistent with the F_{MAX} v N_f performance where the HT2 0° material exhibited the strongest response, with the cast variant performing the worst. In contrast however, such features were not visible in fully reversed R ratios, seen here on Ti-6Al-4V, due to the abrasion of the fracture surfaces as the applied force travels through zero.

Author contributions

The work presented in this paper was carried out as a collaboration between all authors. The research theme was defined by Robert Lancaster, Spencer Jeffs and Gavin Baxter. Robert Lancaster and

Spencer Jeffs prepared the scientific manuscript, Henry Illsley performed the mechanical testing and subsequent failure analysis of Ti-6Al-4V materials whilst Sean Davies undertook a similar study on the C263 variants. David Lewis, Robert Lancaster, Spencer Jeffs, Henry Illsley, Sean Davies and Gavin Baxter co-worked on the discussion and interpretation of the results. All authors have contributed to, seen and approved the final manuscript.

Conflicts of interest

The authors declare no conflict of interest.

Acknowledgments

The current research was funded under the EPSRC Rolls-Royce Strategic Partnership in Structural Metallic Systems for Gas Turbines (grants EP/H500383/1 and EP/H022309/1). The provision of materials and technical support from Rolls-Royce plc. is gratefully acknowledged. We would like to acknowledge the assistance provided by Swansea University College of Engineering *AIM* Facility, which was funded in part by the EPSRC (EP/M028267/1), The European Regional Development Fund through the Welsh Government (80708) and the Ser Solar project via the Welsh Government.

Mechanical tests were performed at Swansea Materials Research and Testing Ltd. (SMaRT). Requests for access to the underlying research data should be directed to the corresponding author and will be considered against commercial interests and data protection.

References

[1] T. DebRoy, H.L. Wei, J.S. Zuback, T. Mukherjee, J.W. Elmer, J.O. Milewski, A.M. Beese, A. Wilson-Heid, A. De, W. Zhang, Additive manufacturing of metallic components – process, structure and properties, Prog. Mater. Sci. 92 (2018) 112–224.

[2] J.J. Lewandowski, M. Seifi, Metal additive manufacturing: a review of mechanical properties, Annu. Rev. Mater. Res. 461 (2016) 151–186.

[3] J. Kameda, X. Mao, Small-punch and TEM-disc testing techniques and their application to characterization of radiation damage, J. Mater. Sci. 27 (4) (Feb. 1992) 983–989.

[4] F. Dobeš, K. Milička, Application of creep small punch testing in assessment of creep lifetime, Mater. Sci. Eng. A 510–511 (2009) 440–443.

[5] B.J. Kim, Y.B. Sim, J.H. Lee, M.K. Kim, B.S. Lim, Application of small punch creep test for Inconel 617 alloy weldment, Procedia Eng. 10 (Jan. 2011) 2579–2584.

[6] R.C. Hurst, R.J. Lancaster, S.P. Jeffs, M.R. Bache, The contribution of small punch testing towards the development of materials for aero-engine applications, Theor. Appl. Fract. Mech. 86 (2016) 69–77.

[7] R.J. Lancaster, H.W. Illsley, G.R. Davies, S.P. Jeffs, G.J. Baxter, Modelling the small punch tensile behaviour of an aerospace alloy, Mater. Sci. Technol. 33 (9) (2017) 1065–1073.

[8] R.V. Prakash, Study of fatigue properties of materials through cyclic automated ball indentation and cyclic small punch test methods, Key Eng. Mater. 734 (2017) 273–284.

[9] R.V. Prakash, Investigation of static and fatigue properties of materials through small specimen test methods, Proceedings of the 3rd International Conference on Small Scale Test Techniques, 2014, pp. 339–347.

[10] CEN Workshop Agreement, CWA 15627: Small Punch Test Method for Metallic Materials, (2007) Brussels, Belgium.

[11] R.J. Lancaster, S.P. Jeffs, H.W. Illsley, C. Argyrakis, R.C. Hurst, G.J. Baxter, Development of a novel methodology to study fatigue properties using the small punch test, Mater. Sci. Eng. A 748 (2018) 21–29.

[12] S. Davies, S. Jeffs, R. Lancaster, G. Baxter, High temperature deformation mechanisms in a DLD nickel superalloy, Materials 10 (5) (2017) 457.

[13] S.J. Davies, S.P. Jeffs, M.P. Coleman, R.J. Lancaster, Effects of heat treatment on microstructure and creep properties of a laser powder bed fused nickel superalloy, Mater. Des. 159 (Dec. 2018) 39–46.

[14] R. Lancaster, G. Davies, H. Illsley, S. Jeffs, G. Baxter, Structural integrity of an electron beam melted titanium alloy, Materials 9 (6) (2016).

[15] A.A. Antonysamy, J. Meyer, P.B. Prangnell, Effect of build geometry on the β-grain structure and texture in additive manufacture of Ti6Al4V by selective electron beam melting, Mater. Char. 84 (2013) 153–168.

[16] T. Vilaro, C. Colin, J.D. Bartout, L. Nazé, M. Sennour, Microstructural and mechanical approaches of the selective laser melting process applied to a nickel-base superalloy, Mater. Sci. Eng. A 534 (Feb. 2012) 446–451.

[17] S. Tammas-Williams, P.J. Withers, I. Todd, P.B. Prangnell, Porosity regrowth during heat treatment of hot isostatically pressed additively manufactured titanium components, Scripta Mater. 122 (Sep. 2016) 72–76.

[18] S. Tammas-Williams, H. Zhao, F. Léonard, F. Derguti, I. Todd, P.B. Prangnell, XCT analysis of the influence of melt strategies on defect population in Ti-6Al-4V components manufactured by Selective Electron Beam Melting, Mater. Char. 102 (2015) 47–61.

[19] E.O. Hall, The deformation and ageing of mild steel: III Discussion of results, Proc. Phys. Soc. B 94 (9) (1951) 747–752.

[20] H.E. Huang, C.H. Koo, Effect of solution-treatment on microstructure and mechanical properties of cast fine-grain CM 247 LC superalloy, Mater. Trans. A 45 (2004) 554–561.

[21] X. You, Y. Tan, S. Shi, J.M. Yang, Y. Wang, J. Li, Q. You, Effect of solution heat treatment on the precipitation behavior and strengthening mechanisms of electron beam smelted Inconel 718 superalloy, Mater. Sci. Technol. 689 (2017) 257–268.

[22] R.C. Reed, The Superalloys: Fundamentals and Applications, Cambridge University Press, 2006.

[23] M. Coleman, H. Alshehri, R. Banik, W. Harrison, S. Birosca, Deformation mechanisms of IN713C nickel based superalloy during Small Punch Testing, Mater. Sci. Eng. A 650 (2016) 422–431.

[24] M. Ramsperger, R.F. Singer, C. Körner, Microstructure of the nickel-base superalloy CMSX-4 fabricated by selective electron beam melting, Metall. Mater. Trans. A 47 (2016) 1469–1480.

[25] S.D. Norris, J.D. Parker, Deformation processes during disc bend loading, Mater. Sci. Technol. 12 (1996) 163–170.

[26] A. Ghosh, N.P. Gurao, Effect of crystallographic texture on ratcheting response of commercially pure titanium, Mater. Des. 115 (Feb. 2017) 121–132.